Conceptual design of heavy ion beam compression using a wedge

Jonathan C. Wong*
Physics Department, The Chinese University of Hong Kong, Hong Kong, China

B. Grant Logan
Lawrence Berkeley National Laboratory, Berkeley, California 94720, USA

Simon S. Yu
Physics Department, The Chinese University of Hong Kong, Hong Kong, China and Lawrence Berkeley National Laboratory, Berkeley, California 94720, USA

(Received 30 January 2014; revised manuscript received 10 July 2015; published 5 October 2015)

Heavy ion beams are a useful tool for conducting high energy density physics (HEDP) experiments. Target heating can be enhanced by beam compression, because a shorter pulse diminishes hydrodynamic expansion during irradiation. A conceptual design is introduced to compress ~100 MeV/u to ~GeV/u heavy ion beams using a wedge. By deflecting the beam with a time-varying field and placing a tailor-made wedge amid its path downstream, each transverse slice passes through matter of different thickness. The resulting energy loss creates a head-to-tail velocity gradient, and the wedge shape can be designed by using stopping power models to give maximum compression at the target. The compression ratio at the target was found to vary linearly with (head-to-tail centroid offset/spot radius) at the wedge. The latter should be approximately 10 to attain tenfold compression. The decline in beam quality due to projectile ionization, energy straggling, fragmentation, and scattering is shown to be acceptable for well-chosen wedge materials. A test experiment is proposed to verify the compression scheme and to study the beam-wedge interaction and its associated beam dynamics, which will facilitate further efforts towards a HEDP facility.

DOI: 10.1103/PhysRevSTAB.18.101301 PACS numbers: 29.27.-a, 41.85.Ew

I. INTRODUCTION

Intense heavy ion beams possess unique capabilities in heating matter for the studies of high energy density physics (HEDP) [1–4] and inertial confinement fusion [5–7]. In target heating experiments, it is important for the beam to deposit its energy rapidly so that the target does not undergo significant expansion during the irradiation [8]. For a small beam radius, the pulse lengths in heavy ion accelerators exceed the hydrodynamic expansion time scale, because the latter diminishes as the spot size decreases [9,10]. Therefore, it is rewarding to compress the beam longitudinally before it hits the target.

Sixtyfold pulse compression for sub-MeV/u beams was demonstrated by the NDCX-I experiment at the Lawrence Berkeley Laboratory [11]. After a head-to-tail velocity gradient was imparted to the beam, all the ions eventually caught up with the beam head as the beam drifted in dense background plasma, where the space charge forces were neutralized. In the experiment, the beam velocity was ramped by induction modules with tailored voltage waveforms. This method is, however, technically difficult and highly expensive in the 100 MeV/u or higher regime.

A low-cost physics design is introduced to generate a velocity tilt for high energy heavy ion beams using a wedge. In the ionization cooling of muons, the method of emittance exchange was proposed to place wedge-shaped absorbers at locations where the transverse positions of the muons would be energy dependent. Higher energy muons would pass through more material than lower energy ones to achieve longitudinal cooling [12,13]. Whereas the above process utilizes the dispersion of muons with different energies, the scheme below makes use of dipoles to sweep the beam across a wedge in time. Different transverse slices of the beam pass through matter of variable thicknesses, which correspond to different energy losses. The resulting velocity gradient allows the beam to drift compress in the neutralizing plasma downstream.

Section II describes the physics design in detail and investigates the decisive factor that determines the longitudinal compression ratio. Section III studies how other physical processes associated with the passage of high energy heavy ions through matter, i.e., projectile ionization, energy straggling, ion fragmentation, and scattering, affect the beam quality. Section IV proposes a straightforward test experiment to verify the compression scheme and to study the beam-wedge interaction and its associated beam

*jonathanwonghk@yahoo.com

Published by the American Physical Society under the terms of the Creative Commons Attribution 3.0 License. Further distribution of this work must maintain attribution to the author(s) and the published article's title, journal citation, and DOI.

dynamics. Section V concludes the findings and outlines further work.

II. LONGITUDINAL BEAM COMPRESSION USING A WEDGE

A physics design is devised to generate a large head-to-tail velocity gradient for ~100 MeV/u to ~GeV/u heavy ion beams at a low cost. First, consider a beam with vanishing spot size and emittance. By deflecting the beam with a time-varying dipole field and placing a wedge amid its path downstream, each transverse slice arrives at the wedge with a different centroid position $\langle y \rangle$. Hence, each transverse slice passes through matter of different thickness, which corresponds to different energy loss. With a well-designed wedge shape, the energy loss can create the desired velocity gradient for the beam, which subsequently drift compresses in a dense plasma that neutralizes the space charge forces.

Figure 1 shows the side view as the beam approaches the wedge. The sweep is defined as the offset in the y position between the centroid of the beam head and that of the tail.

To achieve the maximum compression at the target, where all ions overtake the beam head simultaneously, the ideal velocity gradient imparted onto the beam is

$$\frac{v(y)}{v0} = \frac{l_{\mathrm{drift}}}{l_{\mathrm{drift}} + l_{\mathrm{beam}} \times (1 - \frac{y}{\mathrm{sweep}})}, \tag{1}$$

where l_{drift} is the wedge-to-target drift length, l_{beam} is the beam length, $v0$ is the original beam velocity, y is the ion position, and $v(y)$ is the velocity of the beam ions exiting the wedge at y. Figure 2 is the plot of $v(y)$ versus y for a 20% velocity gradient.

A. Wedge shape

Table I shows, for 1 GeV/u ^{238}U ions, the characteristic thicknesses needed to obtain the specified velocity reduction in different materials. For a given energy loss, the thickness decreases in higher-Z materials.

The ideal velocity gradient given by Eq. (1) determines the energies of the beam ions exiting the wedge at different y positions. The wedge thickness that induces the required energy loss at each y position can be computed with stopping power models to construct the shape of the wedge.

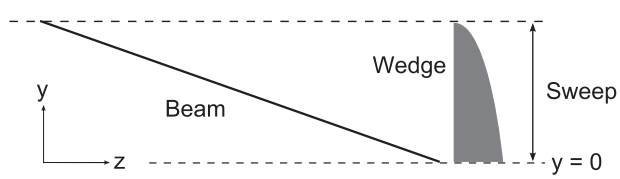

FIG. 1. Side view in real space as a beam with vanishing spot size approaches the wedge.

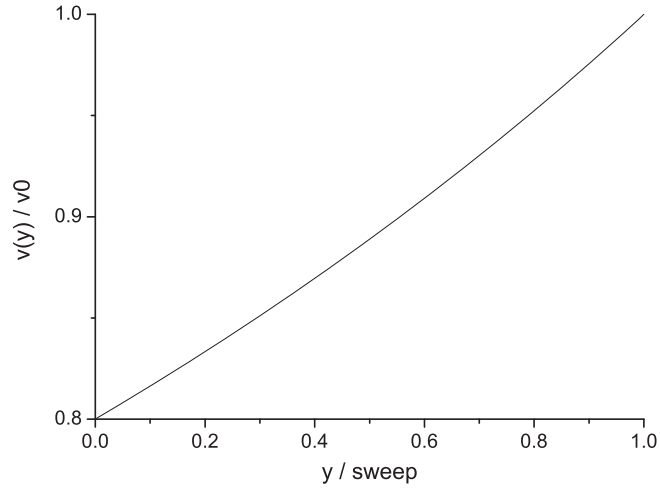

FIG. 2. The ideal velocity of beam ions exiting the wedge at different y positions for a 20% velocity gradient.

A sample wedge generated with the stopping power model of SRIM [14] is shown in Fig. 3.

B. Finite spot size

The previous subsections assume the beam has a vanishing spot size at the wedge. In that case, if longitudinal emittance is ignored, perfect compression is possible at the target. How the relaxation of the spot-size idealization imposes a limit on the maximum compression ratio is investigated below.

When the beam has a finite spot size at the wedge, beam ions in a transverse slice do not get the same energy loss from the wedge, because the thicknesses through which they penetrate differ. In other words, some ions do not get the ideal energy loss due to the finite spot size. Figure 4 shows how the discrepancy depends on the sweep and the spot size.

Ballistic simulations were conducted to investigate how the sweep and the spot size affect the longitudinal compression at the target. The arrangement of the beam is shown in Fig. 5. The beam has a Gaussian radial profile, where 2σ is taken as the effective beam radius, and a Gaussian temporal profile, where 2σ is taken as the beam duration. Each beam ion was given the perfect velocity

TABLE I. The amount of material through which 1 GeV/u ^{238}U ions have to penetrate to achieve the specified exiting velocities, calculated by SRIM [14]. Here $v0 = 0.876c$.

Exiting velocity ($v/v0$)	0.8	0.6	0.4	0.2
Exiting energy (MeV/u)	373.4	163.5	63.1	14.6
Thickness of Li (mm)	168.52	206.97	218.13	221.05
Thickness of C (mm)	36.67	45.03	47.47	48.10
Thickness of Al (mm)	34.22	42.13	44.46	45.08
Thickness of Cu (mm)	11.97	14.76	15.58	15.81
Thickness of Pb (mm)	12.11	14.99	15.86	16.11

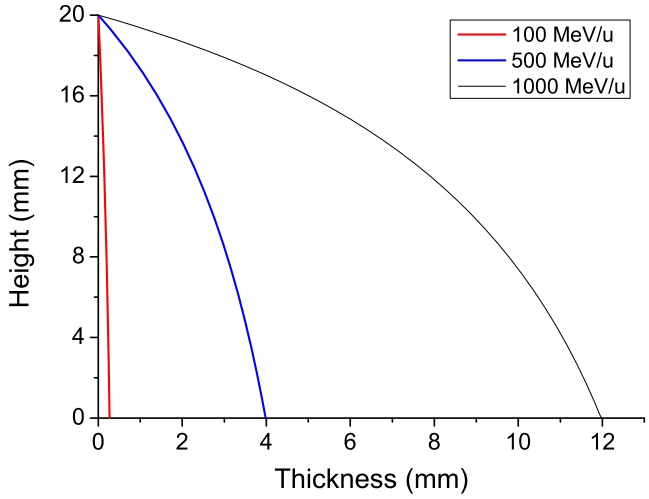

FIG. 3. Side view of the Cu wedge that produces a 20% velocity gradient for ^{238}U beams with the specified energies. The 3D wedge is uniform in the direction into and out of the paper. The height is arbitrary, as it will be designed to match the sweep of the beam.

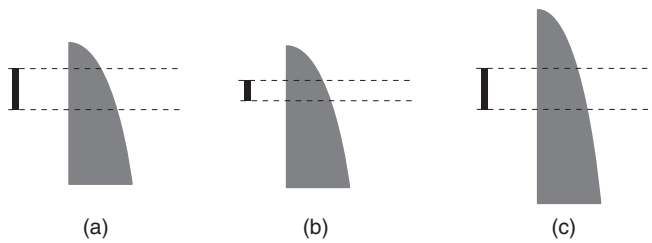

FIG. 4. (a) and (b) show that, for a fixed sweep, the smaller the spot size, the smaller the discrepancy in energy loss within a slice. (a) and (c) show that, for a fixed spot size, the larger the sweep, the smaller the discrepancy in energy loss within a slice.

change according to its y position at the wedge, and the final particle current was measured at the target position. The compression ratio is defined as the ratio between the original and final beam duration. The results, plotted in Fig. 6, show that the compression ratio varies with the dimensionless parameter (sweep/spot radius) at the wedge

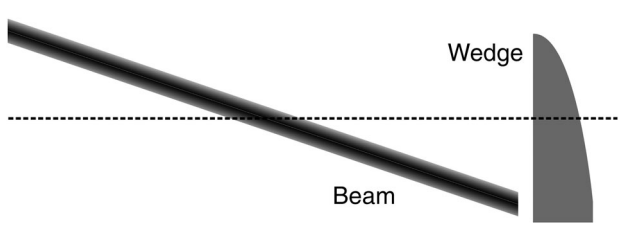

FIG. 5. Side view in real space as a beam with finite spot size approaches the wedge. Outlying beam ions whose y positions are above the centroid of the beam tail or below the centroid of the beam head experience the same energy loss as the respective centroid.

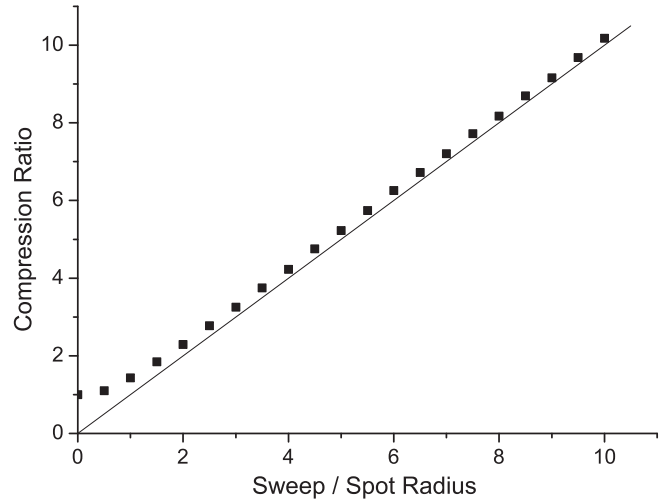

FIG. 6. Simulation results of the compression ratios at the target for different (sweep/spot radius) ratios at the wedge. They can be compared with the straight line which denotes $y = x$.

almost linearly, except when the latter is small, because the compression ratio equals unity when there is no wedge (i.e., sweep $= 0$).

A simple model can explain the relationship between the compression ratio and (sweep/spot radius). The dotted line in Fig. 5 denotes a longitudinal slice of the beam and its path through the wedge. The tail ions of the longitudinal slice undergo exactly the same path as the head ions, except for a delay in time by (slice length$/v0$) = slice duration. The duration of each longitudinal slice is not shortened by the wedge; thus, it is equivalent to the final beam duration at the target.

Figure 7 shows, via simple geometry, that

$$\frac{\text{sweep}}{r_{\text{spot}}} = \frac{l_{\text{beam}}}{l_{\text{slice}}} = \frac{l_{\text{beam}}/v0}{l_{\text{slice}}/v0} = \frac{\tau_i}{\tau_f} = \text{compression ratio} \qquad (2)$$

where l_{beam} is the original beam length, l_{slice} is the length of a longitudinal slice, $v0$ is the original beam velocity, and τ_i and τ_f are the initial and final beam duration, respectively.

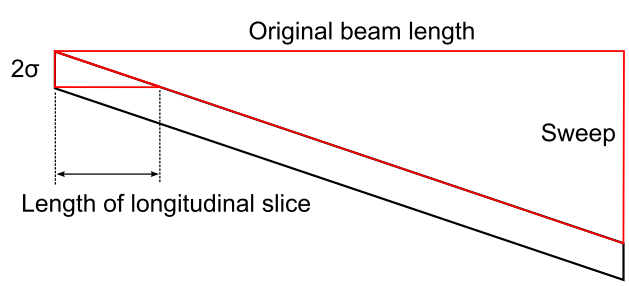

FIG. 7. The boundary of the beam with finite spot size and related geometries.

The model does not account for the outlying ions and is therefore more accurate for larger (sweep/spot radius) when the amount of outlying ions is smaller. This agrees with the trend exhibited in Fig. 6. Since spot size typically is approximately millimeters, 10-time longitudinal compression requires sweep of approximately centimeters.

III. BEAM-WEDGE INTERACTION

The penetration of relativistic heavy ions through matter involves complex processes. Apart from the stopping power and its applications studied in the last section, other physical effects are present which affect the properties of the beam. Projectile ionization, energy loss straggling, ion fragmentation, and scattering are studied in this section. Although the beam quality deteriorates as a result of all these processes, the damage is shown to be acceptable.

A. Charge state

Beam ions of heavy ion accelerators are far from fully stripped, but they will be stripped by the wedge. It is well known that ions with higher energies have a larger average equilibrium charge and narrower equilibrium charge-state distribution when they are penetrating through matter [15]. Since the compression scheme involves ions exiting the wedge at different energies, how their charge states vary is a primary concern. A fit formula by Schiwietz and Grande [16,17] and the code GLOBAL [15] were employed to calculate the equilibrium charge-state distribution of heavy ions in matter at different energies. The results are shown in Table II.

A comparison of the equilibrium thicknesses in Table II and the characteristic thicknesses in Table I shows that the beam ions can attain the equilibrium charge-state distribution in the wedge. According to Table II, in the energy range of interest, the equilibrium charge-state distribution of the ions exiting the wedge is quite uniform regardless of the wedge material. First, the width of the equilibrium charge-state distribution dq is narrow, so ions with the same energy have similar charge states. Second, the average equilibrium charges $\bar{q}$ are little different across vastly different energies. The 0.1 GeV/u ions have a $\bar{q}$ less than 3% smaller than that of 1 GeV/u ions. The small variation in charge states is favorable to beam manipulation downstream.

TABLE II. Average equilibrium charge $\bar{q}$, the width of the equilibrium charge-state distribution dq, and the equilibrium thickness D for 0.1 and 1 GeV/u ^{238}U ions in Li, C, Al, and Cu targets, calculated by using the formula by Schiwietz and the code GLOBAL.

	Schiwietz	GLOBAL	GLOBAL	GLOBAL
Ion energy	$\bar{q}$	$\bar{q}$	dq	D (mm)
(a) Li				
1 GeV/u	91.96	91.28	0.69	20.9
0.1 GeV/u	90.55	89.53	0.72	2.98
(b) C				
1 GeV/u	91.98	91.52	0.61	2.84
0.1 GeV/u	89.82	89.79	0.60	0.58
(c) Al				
1 GeV/u	91.77	91.72	0.49	1.36
0.1 GeV/u	88.84	89.73	0.66	0.44
(d) Cu				
1 GeV/u	91.39	91.85	0.37	0.21
0.1 GeV/u	87.68	88.83	1.09	0.10

B. Energy straggling

Beam ions passing through the same thickness of a material experience fluctuations in their energy losses, the aforementioned charge-state distributions being one of the reasons. Table III shows that energy straggling has little target material dependence. Energy straggling is more severe for beam ions with higher energy losses, because their final kinetic energies (KEs) are smaller and their σ's of energy straggling are larger. Details can be found in Table IV.

As studied in Sec. II, in the wedge compression scheme, a finite spot size at the wedge causes a variation in energy loss within a transverse slice, thereby posing a limit on the compression ratio. For a 60% head-to-tail velocity gradient and $(\mathrm{sweep}/2r_{\mathrm{spot}}) = 10$, the discrepancy in exiting velocity within a transverse slice spans approximately $0.06v0$. The δv due to energy straggling for ions exiting with $0.4v0$ is merely $0.006v0$, and the fluctuations are smaller for ions passing through thinner parts of the wedge. Therefore, energy straggling does not hamper the axial compression severely except for very large velocity gradients.

TABLE III. The σ of energy straggling for 1 GeV/u ^{238}U ions losing the same energy in different target materials, calculated by the code ATIMA [18].

	Li	C	Al	Cu	Pb
σ^{a} (MeV/u)	0.845	0.876	0.891	0.924	0.954
σ^{b} (MeV/u)	3.897	3.919	3.767	3.698	3.482

[a]20% velocity reduction, final KE = 373.4 MeV/u.
[b]80% velocity reduction, final KE = 14.6 MeV/u.

TABLE IV. The σ of energy straggling for 1 GeV/u ^{238}U ions passing through a C target with the specified energy losses, calculated by the code ATIMA.

Final v ($v/v0$)	Final KE (MeV/u)	σ (MeV/u)	$\delta p/p$	$\delta v/v$
0.8	373.4	0.873	0.14%	0.07%
0.6	163.5	1.314	0.43%	0.31%
0.4	63.1	2.069	1.68%	1.47%
0.2	14.6	3.919	12.7%	12.2%

C. Fragmentation

Beam ions may undergo fragmentation in their passage through matter. With vastly different charge-to-mass ratios, angles, and momenta, how the fragments would hit the target is difficult to gauge. The worst-case estimate would be to count fragmented ions as lost.

The empirical parametrization of fragmentation cross sections (EPAX) formula [19] was employed to obtain the sum of all fragmentation cross sections which is the total fragmentation cross section. The sum of all fragmentation cross sections is the total fragmentation cross section. The mean free path λ can be calculated as follows:

$$\lambda = \frac{A_t}{\rho N_A \sigma_{\text{total}}}, \tag{3}$$

where A_t and ρ are the mass number and density of the target material, respectively, N_A is the Avogadros number, and σ_{total} is the total cross section.

The probability of fragmentation P is given by

$$P = 1 - \exp\left(-\frac{x}{\lambda}\right), \tag{4}$$

where λ is the mean free path and x is the length of the material penetrated. The probability of fragmentation P exhibits two trends:

(i) Given the same energy loss, P is larger for lower-Z materials as shown in Table V.

(ii) P increases as the ion energy increases. Beam ions over 100 MeV/u are in the limiting fragmentation regime where the fragmentation cross sections are energy independent [21]. As the ion energy increases, a thicker layer is required to deliver the same percentage velocity reduction, while the mean free path remains constant. Hence, P increases.

D. Scattering

The results in Table VI show that, for the same energy loss, scattering increases for higher-Z wedge materials.

TABLE V. The mean free path λ and probability of fragmentation P for 1 GeV/u ^{208}Pb ions penetrating through matter that causes a 20% velocity reduction, calculated by using the EPAX formula with the aid of the program LISE++ [20]. The exiting energy is 373 MeV/u.

	λ (mm)	Thickness (mm)	P
Li	116.32	164.80	0.758
C	44.91	36.40	0.555
Al	75.73	33.68	0.359
Cu	47.38	11.66	0.218
Pb	98.29	11.72	0.112

TABLE VI. Scattering angles for 1 GeV/u ^{238}U ions penetrating through matter that causes a 20% velocity reduction, calculated by the codes SRIM and ATIMA. The exiting energy is 373 MeV/u. Statistical analysis of the SRIM data was aided by the SRIM supporting software modules [22].

	Thickness (mm)	SRIM θ_{rms} (mrad)	ATIMA θ_{rms} (mrad)
Li	168.53	1.366	1.995
C	36.67	1.875	2.244
Cu	11.97	4.895	4.592
Pb	12.11	7.846	7.465

For rms emittance and normalized edge emittance

$$\varepsilon^2 = \langle x^2\rangle\langle x'^2\rangle - \langle xx'\rangle^2,$$
$$\varepsilon_N = 4\gamma\beta\varepsilon,$$

the change in ε_N due to the wedge has two contributions: (i) β and γ decrease as the beam loses energy; (ii) rms emittance ε increases due to scattering. The latter can be calculated by using statistical arguments. Assume the wedge changes only the angles of the ions and not their positions:

$$x_1 = x_0,$$
$$x_1' = x_0' + \theta,$$

where θ is the scattering angle. Subscript 0 denotes quantities before the ions hit the wedge, and subscript 1 denotes those of the ions exiting the wedge. Using the fact that θ is uncorrelated with x_0 and x_0' and that θ averages to zero, one obtains

$$\langle {x_1}^2\rangle\langle x_1'^2\rangle - \langle x_1 x_1'\rangle^2 = \langle {x_0}^2\rangle\langle x_0'^2\rangle - \langle x_0 x_0'\rangle^2 + \langle {x_0}^2\rangle\langle\theta^2\rangle. \tag{5}$$

Therefore, a small beam radius at the wedge serves two purposes: (i) to reduce the sweep required to generate a large compression ratio according to Eq. (2) and (ii) to limit the rms-emittance growth caused by scattering.

The following example shows that the change in ε_N is acceptable for typical beam parameters. Consider a 1 GeV/u ^{238}U beam with normalized edge emittance $\varepsilon_{N-\text{old}} = 100$ mm mrad which passes through 12.11 mm-thick Pb to acquire 20% velocity reduction.

Using Eq. (5) and taking $\langle {x_0}^2\rangle = 1$ mm^2 and $\langle\theta^2\rangle = 61.6$ mrad^2 according to Table VI, one obtains the emittance after the wedge $\varepsilon_{N-\text{new}} = 62.3$ mm mrad.

E. Selecting an appropriate wedge material

Since the width of the charge-state distribution and the energy straggling have little target dependence, the choice

TABLE VII. Examples of how the beam quality declines as it passes through well-chosen materials to achieve the specified velocity reduction. The quantities are estimated by using the EPAX formula and the codes GLOBAL and ATIMA.

Ion	$^{208}Pb^{82+}$	$^{208}Pb^{82+}$
Ion energy	1 GeV/u	100 MeV/u
v_{final}/v_0	0.9	0.9
p_{final}/p_0	0.541	0.881
Final energy (MeV/u)	582.8	78.5
Wedge material, thickness in mm	Pb, 9.26	C, 0.502
Energy straggling σ (MeV/u)	0.752	0.050
Angular straggling θ_{rms} (mrad)	3.87	1.19
Mean charge state $\bar{q}$	81.90	79.93
Width of charge-state distribution dq	0.30	0.54
Fragmentation probability	9.05%	1.11%

of wedge material often boils down to a compromise between fragmentation and scattering. While the magnitude of the velocity gradient may also influence the decision, a simple guideline would be to use higher-Z wedges for ion energies approaching 1 GeV/u to minimize the fragmentation and to use lower-Z wedges for ion energies closer to 100 MeV/u to reduce the scattering when the fragmentation is less significant.

The examples in Table VII show that, for well-chosen wedge materials, the decline in beam quality is tolerable.

It should be noted that the results presented above concern beam ions passing through the thickest part of the wedge. They are not representative of the whole beam, because there is a range of energy losses for ions in the beam, and the detrimental effects decrease in magnitude for smaller energy losses. For example, the fragmentation probability for a particle in the beam, as opposed to one in the slice passing through the thickest part, is 5.9% and 0.7%, respectively. The decline in the quality of the entire beam should be gauged in this regard.

IV. TEST EXPERIMENT

A test experiment is proposed for heavy ion beam compression using a wedge. The experiment has two objectives: (i) to verify the physics design for longitudinal beam compression; (ii) to enhance quantitative understanding of the beam-wedge interaction and its associated beam dynamics downstream of the wedge, which is crucial to the subsequent design of the final focusing system. The test experiment will be the basis for further efforts to implement the wedge compression scheme in a HEDP facility.

A. Experimental setup

The basic setup can be found in Fig. 8. Because no target experiment is involved, a low current beam can be used and no final focusing element is required. The dipoles generate a large (sweep/spot size) ratio at the wedge. Wedges made

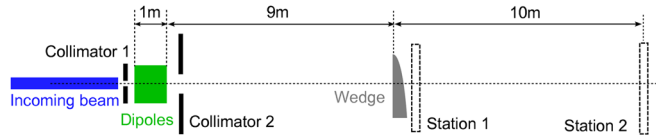

FIG. 8. Schematic layout of the test experiment. The collimators are optional, and the dimensions listed are for reference only.

of different materials can be tried to check the wedge selection guidelines given in Sec. II E.

Diagnostics elements are placed at station 1 and station 2. Current measurements at station 2, the target position, can determine the longitudinal compression ratio of the beam. Station 1 is installed closely behind the wedge to obtain detailed knowledge of the beam-wedge interaction and the related beam dynamics. Beam transverse position measurements can check the performance of the dipoles. The beam kinetic energy profile can be compared with the stopping power and straggling predicted by the models employed. Measurements of the beam line charge density, ion fragments, and the beam emittance can shed light on the projectile ionization, fragmentation, and scattering due to the wedge, respectively.

B. Beam chopper options

The beam head has the slowest velocity after exiting the wedge. A variation of Eq. (1) reveals that v_{head}, the velocity of the beam head after the wedge, is

$$v_{head} = v0 \times \frac{l_{drift2}}{l_{drift2} + l_{beam}}, \tag{6}$$

where l_{drift2} is the wedge-to-target drift length and l_{beam} is the beam length arriving at the wedge. v_{head} is preferably no less than $0.5v0$, because a large velocity reduction incurs a severe decline in the beam quality due to the beam-wedge interaction. Larger energy variation among the beam ions also renders the final focusing more difficult. $v_{head} > 0.5v0$ requires $l_{beam} < l_{drift2}$, which may be difficult to achieve without shortening the incoming beam because pulse lengths from an accelerator are easily longer than 20 m (e.g., a 100 ns, 500 MeV/u beam is 23.1 m long).

A collimator (collimator 2 in Fig. 8) can be used in combination with the dipoles to chop the head and tail of the incoming beam so that l_{beam} at the wedge becomes smaller than l_{drift2}. As the dipoles deflect the beam, the aperture is designed to let only a portion of the transverse slices (ideally, the most populated ones) pass. The other beam ions hit the collimator and are stopped completely. Hence, the beam is chopped, and, for a fixed l_{drift2}, longitudinal compression can be tested with a smaller velocity gradient.

Similarly, a collimator (collimator 1 in Fig. 8) with a variable hole size can be used to reduce the current and

emittance of the incoming beam. That minimizes the spot size and increases the (sweep/spot size) ratio at the wedge.

C. Dipole

For an incoming beam without an original head-to-tail velocity gradient, a time-varying magnetic field is required to deflect each transverse slice in different angles. The resulting sweep at the wedge is given by the following formula:

$$\text{sweep} = \frac{q}{\gamma m} l_{\text{dipole}} \times \frac{l_{\text{beam}}}{v0} \frac{dB}{dt} \times \frac{l_{\text{drift1}}}{v0}, \tag{7}$$

where q and m are the charge and mass of the beam ions, respectively, l_{drift1} is the dipole-to-wedge drift length, and l_{dipole} is the total dipole length. The second term is the difference in B field experienced by the head and tail ions. The product of the first two terms gives the difference in v_y between the head and tail ions. That multiplied by the drift time gives the sweep at the wedge. Assuming a spot size of approximately millimeters, a sweep of approximately centimeters is required to achieve 10-time compression. Using the sample beam ions 235 MeV/u $^{129}\text{Xe}^{29+}$ available from the Cooler-Storage-Ring at Institute of Modern Physics-Lanzhou [23], for sweep = 40 mm, beam duration $\tau = 50$ ns, $l_{\text{drift1}} = 9$ m, and $l_{\text{dipole}} = 1$ m, one obtains

$$\frac{dB}{dt} \approx 10^6 \times \frac{11 \times \text{sweep[mm]}}{l_{\text{drift1}}[\text{m}] \times l_{\text{dipole}}[\text{m}] \times \tau[\text{ns}]} \approx 1.0 \times 10^6\ \text{Ts}^{-1}.$$

The generation of such fast-changing fields requires a dipole design with low inductance so as to minimize the operating voltage. The preliminary design below shows that the parameters are achievable.

The dipole in Fig. 9 is effectively the superposition of two cylinders with uniform axial current densities that are equal in magnitude but opposite in direction [24]. The overlapping volume is made hollow, and the current on each side is carried by a set of single-turn coils. The configuration produces a uniform magnetic field $B = \frac{d}{2}\mu_0 J$ in the gap. Detailed calculations of the inductance and the required voltage can be found in the Appendix. For $R = 11$ mm and $d = 2$ mm, the dipole with a 2 cm aperture has inductance per meter $= 2.2 \times 10^{-7}$ H m^{-1}, and the required voltage for $l_{\text{dipole}} = 1$ m is $V = 3.8$ kV. Last but not least, the 1 m dipole can be split into multiple shorter sections run by separate circuits if lower voltages are preferred.

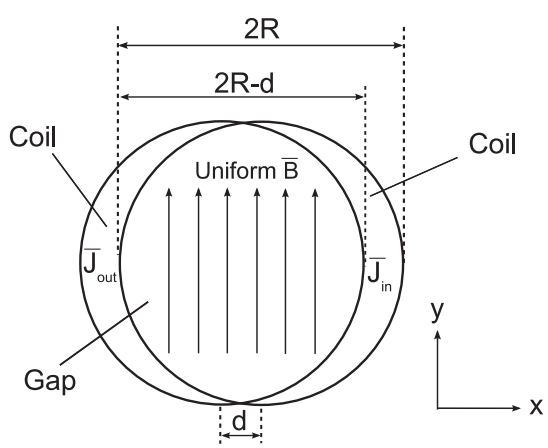

FIG. 9. Schematic diagram of the front view of the dipole. The dipole's length extends in the z direction. The current of the two sets of coil flow into and out of the paper, respectively.

V. CONCLUSION

The paper has introduced a conceptual design to compress high energy heavy ion beams using a wedge. As the first paper on a new concept, its major goal is to show the workings and feasibility of the scheme via a study of the longitudinal beam dynamics and the beam-wedge interactions. In addition, a test experiment has been proposed to verify the principle of beam compression using a wedge and to enhance understanding of the beam-wedge interaction and its associated beam dynamics. The experiment will be an important step towards the realization of the scheme.

The concept of the wedge compression scheme was described in detail in Sec. II. A study of the longitudinal dynamics revealed how the wedge shapes can be designed by using stopping power models. The fundamental relation which states that the compression ratio at the target $\approx(\text{sweep}/r_{\text{spot}})$ at the wedge was established by particle simulations and explained by a simple analytic model. The result entails that the beam has to be relatively well focused at the wedge, and an approximately centimeter sweep is required to achieve tenfold longitudinal compression. Although generating an approximately centimeter sweep may require fast-changing fields with dB/dt of the order 10^6 T/s, the design of a low-inductance dipole in the Appendix showed that the engineering challenges can be met.

In Sec. III, four physical processes that occur when heavy ions traverse matter—projectile ionization, energy straggling, fragmentation, and scattering—were investigated with special emphasis on their dependence on the projectile energy and target material. Concrete examples were displayed in Sec. III E to demonstrate that the decline in beam quality due to beam-wedge interactions is acceptable for well-chosen wedge materials.

To further reduce the detrimental effects of projectile ionization, it is worthwhile to explore whether there are efficient strippers that can be installed downstream of the wedge to make the charge-state distribution of the post-wedge beam more uniform. Another issue that warrants more discussion is the correlation among the four physical processes. In this paper, the physical processes are

investigated independently and the correlation among them is neglected. Since the processes under question are single-particle effects, the correlation is a higher order correction that should not affect the conclusion regarding the decline in beam quality. To aid the eventual optimization of the scheme, the correlation can be investigated as part of the test experiment or by using well-established particle codes such as GEANT4 [25] or FLUKA [26].

To implement the scheme in HEDP target experiments, apart from adding a neutralizing plasma for drift compression, reverse dipoles and a final focusing system should be installed before and after the wedge, respectively. The dipoles deflect each transverse slice of the incoming beam in different angles. If no correction is made, the centroid of each slice will arrive at target at a different y position. The reverse dipoles bend all transverse slices back so that their centroids converge at the target. The reverse dipoles should be placed immediately upstream of the wedge in order not to undo the sweep generated by the dipoles. The reverse dipoles have parameters similar to those of the dipoles and should not pose additional manufacturing difficulties.

The velocity gradient that generates the longitudinal beam compression and the charge-state distribution attained at the wedge impose a large chromaticity onto the beam that makes transverse focusing more challenging. Possible final focusing systems which can accommodate the postwedge beam include time-varying magnets, lithium [27] or adiabatic plasma [28] lens, foil focusing [29], and achromatic magnetic systems [30].

A point design of the final focusing system has been completed as part of the thesis of Wong [31]. The design employs dipoles and quadrupoles with time-varying fields to achieve focusing and tenfold bunching simultaneously. Although the beam spot at the target is inevitably degraded by the beam manipulation and beam-wedge interactions, simulations of the time-dependent particle distribution at the target show that the point design can boost an accelerator facility's capacity for HEDP experiments and that a warm dense matter regime with very short pulses is attainable with near-term beam parameters. Details of the design will be reported in another publication in due course.

ACKNOWLEDGMENTS

We express our gratitude to Dr. John J. Barnard (LLNL), Dr. Alex Friedman (LLNL), Dr. Enrique Henestroza (LBNL), Professor Steven M. Lund (MSU), and Professor Yongtao Zhao (IMP-Lanzhou) for many fruitful discussions and to Mr. Louis L. Reginato (LBNL) and Mr. William L. Waldron (LBNL) for their help in the preliminary design of the time-varying dipoles.

APPENDIX: DIPOLE INDUCTANCE

Please refer to Fig. 9 for the diagram. To minimize the inductance, the current on each side of the gap is carried by a set of single-turn coils and each set belongs to a separate circuit. The inductance of either one of the circuits is calculated as follows. The width and area of the gap are

$$W_{\mathrm{gap}} = 2R - d,$$
$$A_{\mathrm{gap}} = 2R^2 \times \cos^{-1}\left(\frac{d}{2R}\right) - \frac{d}{2} \times \sqrt{4R^2 - d^2}.$$

The current in the circuit is

$$I = J \times A_{\mathrm{coil}} = \frac{2B}{\mu_0 d} A_{\mathrm{coil}}, \tag{A1}$$

where $A_{\mathrm{coil}} = \pi R^2 - A_{\mathrm{gap}}$ is the coil area on one side.

The energy stored in the magnetic field U has contributions from the gap, the coil, and the yoke. Neglecting U_{coil}, consider

$$U_{\mathrm{gap}} = \frac{B^2}{2\mu_0} \times \frac{A_{\mathrm{gap}}}{2} \times l_{\mathrm{dipole}},$$
$$U_{\mathrm{yoke}} = \frac{B^2}{2\mu_0\mu_r} \times \frac{A_{\mathrm{yoke}}}{2} \times l_{\mathrm{dipole}}.$$

Both A_{gap} and A_{yoke} are divided by 2, because there are two circuits and only one of them is being considered. Since $\mu_r \sim 1000$, $U_{\mathrm{gap}} \gg U_{\mathrm{yoke}}$. Thus, the inductance of the circuit L is

$$L = \frac{2U}{I^2} \approx \frac{2U_{\mathrm{gap}}}{I^2} = \frac{\mu_0 d^2}{8} \frac{A_{\mathrm{gap}} \times l_{\mathrm{dipole}}}{A_{\mathrm{coil}}^2}, \tag{A2}$$

which is solely determined by the geometry as expected. For $R = 11$ mm, $d = 2$ mm:

$$\text{inductance per meter} = 2.2 \times 10^{-7}\ \mathrm{H\,m^{-1}},$$
$$L \times \frac{dI}{dt} = 3.8 \times l_{\mathrm{dipole}}[\mathrm{m}] \times \frac{dB}{dt}[10^6\ \mathrm{Ts^{-1}}]\ \mathrm{kV}.$$

It can be seen that it is possible to generate dB/dt that amounts to 10^6 T/s without exceeding an operating voltage of 10 kV.

[1] N. A. Tahir, A. Shutov, D. Varentsov, P. Spiller, S. Udrea, D. H. H. Hoffmann, I. V. Lomonosov, J. Wieser, M. Kirk, R. Piriz, V. E. Fortov, and R. Bock, Phys. Rev. ST Accel. Beams **6**, 020101 (2003).

[2] N. A. Tahir, C. Deutsch, V. E. Fortov, V. Gryaznov, D. H. H. Hoffmann, M. Kulish, I. V. Lomonosov, V. Mintsev, P. Ni, D. Nikolaev, A. R. Piriz, N. Shilkin, P. Spiller, A. Shutov, M. Temporal, V. Ternovoi, S. Udrea, and D. Varentsov, Phys. Rev. Lett. **95**, 035001 (2005).

[3] D. Hoffmann, A. Blazevic, P. Ni, O. Rosmej, M. Roth, N. Tahir, A. Tauschwitz, S. Udrea, D. Varentsov, K. Weyrich, and Y. Maron, Laser Part. Beams **23**, 47 (2005).
[4] V. E. Fortov, D. H. Hoffmann, and B. Y. Sharkov, Phys. Usp. **51**, 109 (2008).
[5] N. Tahir and K. Long, Nucl. Fusion **23**, 887 (1983).
[6] G. Magelssen, Nucl. Fusion **24**, 1527 (1984).
[7] A. R. Piriz, Plasma Phys. Controlled Fusion **29**, 565 (1987).
[8] N. A. Tahir, D. H. H. Hoffmann, J. A. Maruhn, K.-J. Lutz, and R. Bock, Phys. Plasmas **5**, 4426 (1998).
[9] N. A. Tahir, A. Kozyreva, P. Spiller, D. H. H. Hoffman, and A. Shutov, Phys. Plasmas **8**, 611 (2001).
[10] N. A. Tahir, A. Kozyreva, P. Spiller, D. H. H. Hoffmann, and A. Shutov, Phys. Rev. E **63**, 036407 (2001).
[11] P. K. Roy, S. S. Yu, E. Henestroza, A. Anders, F. M. Bieniosek, J. Coleman, S. Eylon, W. G. Greenway, M. Leitner, B. G. Logan, W. L. Waldron, D. R. Welch, C. Thoma, A. B. Sefkow, E. P. Gilson, P. C. Efthimion, and R. C. Davidson, Phys. Rev. Lett. **95**, 234801 (2005).
[12] R. Palmer, V. Balbekov, J. S. Berg, S. Bracker, L. Cremaldi, R. C. Fernow, J. C. Gallardo, R. Godang, G. Hanson, A. Klier, and D. Summers, Phys. Rev. ST Accel. Beams **8**, 061003 (2005).
[13] D. Neuffer, Nucl. Instrum. Methods Phys. Res., Sect. A **532**, 26 (2004).
[14] J. F. Ziegler, M. Ziegler, and J. Biersack, Nucl. Instrum. Methods Phys. Res., Sect. B **268**, 1818 (2010).
[15] C. Scheidenberger, T. Sthlker, W. Meyerhof, H. Geissel, P. Mokler, and B. Blank, Nucl. Instrum. Methods Phys. Res., Sect. B **142**, 441 (1998).
[16] G. Schiwietz and P. Grande, Nucl. Instrum. Methods Phys. Res., Sect. B **175–177**, 125 (2001).
[17] G. Schiwietz, K. Czerski, M. Roth, F. Staufenbiel, and P. Grande, Nucl. Instrum. Methods Phys. Res., Sect. B **225**, 4 (2004).
[18] http://web-docs.gsi.de/~weick/atima/.
[19] K. Sümmerer, Phys. Rev. C **86**, 014601 (2012).
[20] O. Tarasov and D. Bazin, Nucl. Instrum. Methods Phys. Res., Sect. B **266**, 4657 (2008).
[21] K. Sümmerer and B. Blank, Phys. Rev. C **61**, 034607 (2000).
[22] M. Pavlovi and I. Strak, Nucl. Instrum. Methods Phys. Res., Sect. B **257**, 601 (2007).
[23] Y. Zhao, G. Xiao, H. Xu, H. Zhao, J. Xia, G. Jin, X. Ma, Y. Liu, Z. Yang, P. Zhang, Y. Wang, D. Li, H. Zhao, W. Zhan, Z. Xu, D. Zhao, F. Li, and X. Chen, Nucl. Instrum. Methods Phys. Res., Sect. B **267**, 163 (2009).
[24] I. I. Rabi, Rev. Sci. Instrum. **5**, 78 (1934).
[25] J. Allison, K. Amako, J. Apostolakis, H. Araujo, P. Dubois, M. Asai, G. Barrand, R. Capra, S. Chauvie, R. Chytracek, G. Cirrone, G. Cooperman, G. Cosmo, G. Cuttone, G. Daquino, M. Donszelmann, M. Dressel, G. Folger, F. Foppiano, J. Generowicz, V. Grichine, S. Guatelli, P. Gumplinger, A. Heikkinen, I. Hrivnacova, A. Howard, S. Incerti, V. Ivanchenko, T. Johnson, F. Jones, T. Koi, R. Kokoulin, M. Kossov, H. Kurashige, V. Lara, S. Larsson, F. Lei, O. Link, F. Longo, M. Maire, A. Mantero, B. Mascialino, I. McLaren, P. Lorenzo, K. Minamimoto, K. Murakami, P. Nieminen, L. Pandola, S. Parlati, L. Peralta, J. Perl, A. Pfeiffer, M. Pia, A. Ribon, P. Rodrigues, G. Russo, S. Sadilov, G. Santin, T. Sasaki, D. Smith, N. Starkov, S. Tanaka, E. Tcherniaev, B. Tome, A. Trindade, P. Truscott, L. Urban, M. Verderi, A. Walkden, J. Wellisch, D. Williams, D. Wright, and H. Yoshida, IEEE Trans. Nucl. Sci. **53**, 270 (2006).
[26] A. Ferrari, P. Sala, A. Fasso, and J. Ranft, CERN-2005-10 (2005), INFN/TC_05/11, SLAC-R-773.
[27] F. Bieniosek and K. Anderson, in *Proceedings of the 15th Particle Accelerator Conference, PAC-1993, Washington, DC, 1993* (IEEE, New York, 1993), Vol. 4, pp. 3163–3165.
[28] S. Yu, S. Eylon, T. Fessenden, E. Henestroza, R. Lafever, W. Leemans, R. Petzoldt, D. Ponce, M. Vella, R. Moir, W. Sharp, R. Peterson, M. Sawan, and A. Tauschwitz, Nucl. Instrum. Methods Phys. Res., Sect. A **415**, 174 (1998).
[29] S. M. Lund, R. H. Cohen, and P. A. Ni, Phys. Rev. ST Accel. Beams **16**, 044202 (2013).
[30] C. Olson, in *Proceedings of the 1988 Linear Accelerator Conference, Williamsburg, VA, 1988* (JP Scientific Ltd, Nantwich, 2013), pp. 34–37, http://epaper.kek.jp/l88/papers/mo3-03.pdf.
[31] C. Y. J. Wong, M.Phil. thesis, The Chinese University of Hong Kong, 2015.